Spiral-Bevel Geometry and Gear Train Precision

Faydor L. Litvin* and John J. Coy†

Spiral-bevel gears have widespread applications in the transmission systems of helicopters, airplanes, trucks, automobiles and many other machines. Some of the major requirements in almost all the fields of application for transmissions are (1) improved life and reliability, (2) reduction in overall weight (i.e., a larger power-to-weight ratio) without compromising the strength and efficiency during the service life, and (3) reduction in the transmission noise.

Spiral-bevel gears used in practice are normally generated with approximately conjugate tooth surfaces by using special machine and tool settings. Therefore, designers and researchers cannot solve the Hertzian contact stress problem and define the dynamic capacity and contact fatigue life (ref. 1) until these settings are calculated. The geometry of gear tooth surfaces is very complicated and the determination of principal curvatures and principal directions of tooth surfaces necessary for calculating the Hertz stress is a very hard problem.

Baxter (refs. 2 and 3), Litvin (refs. 4 to 7), Litvin and Gutman (refs. 8 and 9) and Wildhaber (ref. 10) completed works dealing with the theory of gearings as well as with the theory of spiral bevel gears. Coy, Townsend, and Zaretsky (ref. 1), Coy, Rohn, and Loewenthal (ref. 11) completed work dealing with dynamic capacity and surface fatigue life of gears. Townsend, Coy, and Hatvani (ref. 12) analyzed failures of a helicopter transmission.

In this paper a novel approach to the study of the geometry of spiral bevel gears and to their rational design is proposed. The nonconjugate tooth surfaces of spiral-bevel gears are, in theory, replaced (or approximated) by conjugated tooth surfaces. These surfaces can be generated (1) by two conical surfaces rigidly connected with each other and in linear tangency along a common generatrix of tool cones, and (2) by a conical surface and a surface of revolution in linear tangency along a circle.

We can imagine that four surfaces are in mesh: two of them are tool surfaces Σ_F and Σ_k; and two are gear tooth surfaces Σ_1 and Σ_2. Surfaces Σ_F and Σ_1 are in linear contact, and contact lines of different form appear on the contacting surfaces in the process of meshing of the generating and the generated surfaces. The same can be said about the contact of surfaces Σ_K and Σ_2. Surfaces Σ_F and Σ_K are rigidly connected and move in the process of meshing as one body. Surfaces Σ_1 and Σ_2 are in point contact and the point of their contact moves along these surfaces in the process of meshing. Surfaces Σ_1 and Σ_2 are hypothetical conjugate tooth surfaces which approximate the actual nonconjugate tooth surfaces.

The determination of surface principal curvatures and directions is a complicated problem. Therefore, a new approach to the solution of these is proposed in this presentation. In this approach direct relationships between the principal curvatures and directions of the tool surface and those of the generated gear surface are obtained. Therefore, the principal curvatures and directions of gear-tooth surface are obtained without using the complicated equations of these surfaces. This makes it easier to apply previously worked out methods for calculating life and reliability for spur and helical gears and traction-drive contacts to the spiral-bevel gear problem.

A general theory of the train kinematical errors exerted by manufacturing and assembly errors is discussed. Two methods for the determination of the train kinematical errors can be worked out: (1) with the aid of a computer, and (2) with an approximate method. Results from noise and vibration measurement conducted on a helicopter transmission are used to illustrate the principals contained in the theory of kinematical errors.

---

*University of Illinois at Chicago Circle.

†NASA Lewis Research Center.

Spiral-Bevel Geometry

Figure 1 shows the generating gear g and the member-spiral bevel gear 2 in mesh by cutting. The generating gear rotates about the axis x_f, and the member-gear rotates about the axis z_2. Axes x_f and z_2 form an angle $90° + (\gamma_2 - \Delta_2)$, where γ_2 is the pitch cone angle and Δ_2 is the addendum angle Δ_2 of the member gear 2.

Figure 2 shows the generating gear g and the pinion in mesh by cutting. The axes of rotation x_f and z_1 form an angle $90° - (\gamma_1 - \Delta_1)$, where γ_1 is the pitch-cone angle and Δ_1 is the addendum angle of the pinion 1. It is assumed that gears 1 and 2 rotate in the train about perpendicular axes.

Surfaces of gears 1 and 2 can be generated as conjugated ones if axis z (fig. 3) is an instantaneous axis of rotation in relative motion for all four gears (for gears 1 and 2 and two generating gears). This requirement cannot be fulfilled for spiral bevel gears because the axes of rotation of the generating gears do not coincide with each other but form an angle $\Delta_1 + \Delta_2$ (fig. 3). Therefore, special machine settings by pinion 1 cutting are applied (fig. 2): axes of rotation x_f and z_1 do not intersect with each other and are dislocated by ΔL_1 and ΔE_1 in two perpendicular directions (ΔE_1 is not shown in fig. 2).

The novel approach to the study of the geometry of spiral-bevel gears is based on the substitution of nonconjugated tooth surfaces by conjugated ones, which can be realized in the following two ways or versions. It is well known that the generating surface for spiral-bevel gears is conical (fig. 4). The first version of spiral-bevel geometry is based on the following propositions: (a) two generating conical surfaces are in linear tangency along a common generatrix of both cones (fig. 5); (b) it can be imagined that two generating surfaces are rigidly connected with each other and rotate as one body by gear generation. The surfaces of the generated gears will therefore be in point tangency. The point of contact of the gear surfaces in mesh moves along the common generatrix of the tool cones. This imaginary way of gear meshing results in elliptical-shaped Hertzian contacts which move across the tooth surfaces in the profile direction.

The second version of the spiral-bevel geometry is based on these propositions: (1) One of the generating surfaces is conical, and the other is a surface of revolution (fig.6); (2) both generating surfaces are in linear tangency along a circle of radius r_d; (3) it is assumed that both generating surfaces are rigidly connected and rotate as one body by gear generation.

Surfaces of generated gears with geometry II will also be in point contact. The point of contact between the gear surfaces in mesh moves along the circle of radius r_d (fig. 6). This second version of gear generation provides that motion of the Hertzian ellipse contact will be along the gear tooth surface in the longitudinal direction. The advantages of spiral-bevel geometry II that are possible to achieve are improved conditions of lubrication and increased contact ratio.

Figure 7 shows a generating surface Σ_d which is covered with lines of contact. The generating and generated surfaces are in instantaneous contact at one of these lines. The point of instantaneous

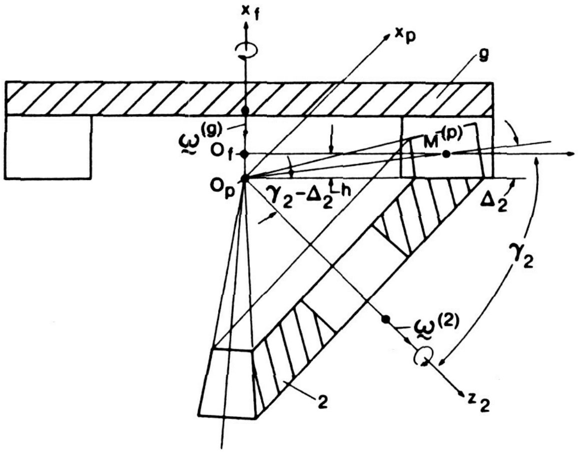

Figure 1. - Generating gear and member gear.

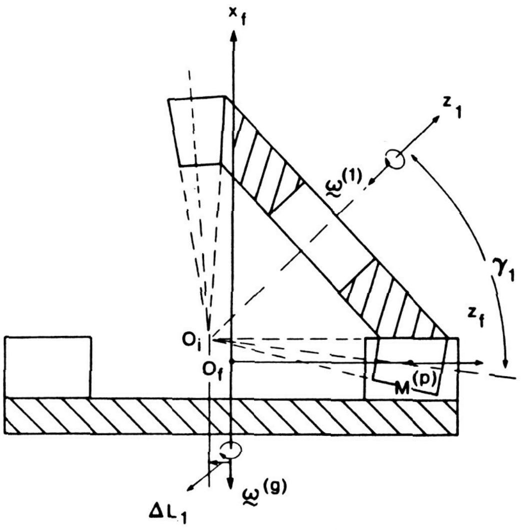

Figure 2. - Generating gear and pinion.

contact of gear surfaces is the point of intersection of the corresponding contact line with the tool cone generatrix (fig. 7). This generatrix is the line of contact of two tool cones for gears with the geometry I. An analogous picture pertains for gear geometry II, but the contact point between the gear surfaces is the point of intersection of the instantaneous contact line with the circle of radius r_d, which is the line of tangency of the two tool surfaces (fig. 6).

The analytical representation of the gear surface contact condition is based on the proposition that radii-vectors and unit normals of surfaces coincide at the contact point, M (fig. 8).

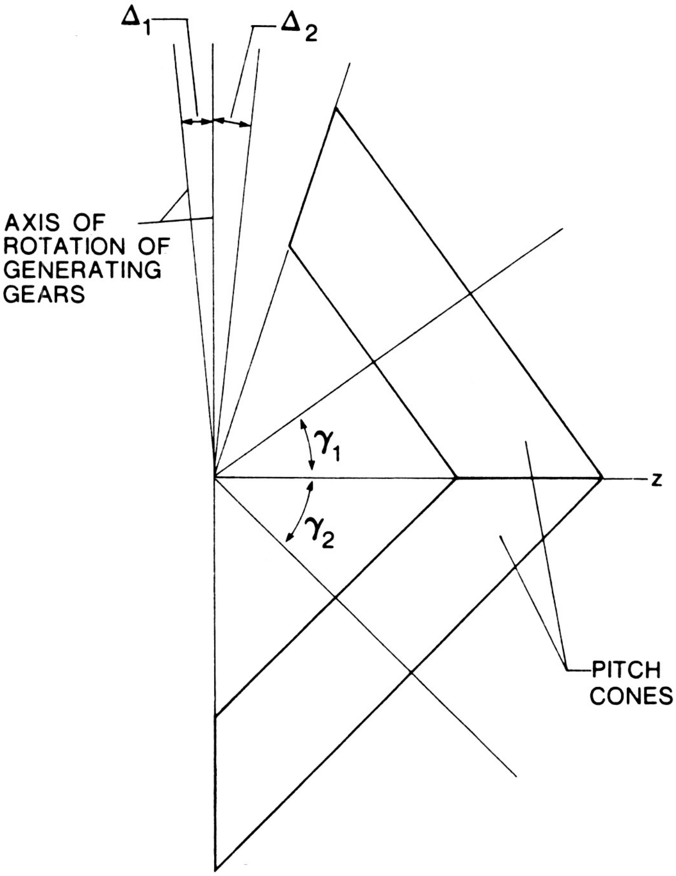

Figure 3. - Axes of rotation of generating gears and member gears.

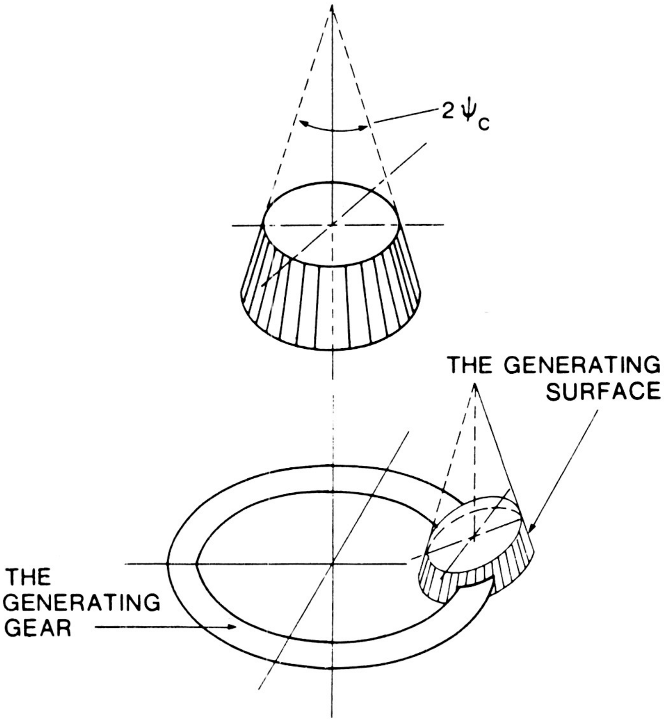

Figure 4. - Tool cone and generating gear.

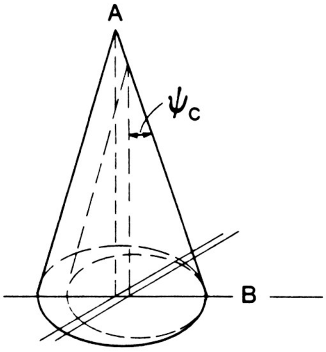

Figure 5. - Generating surfaces for geometry I.

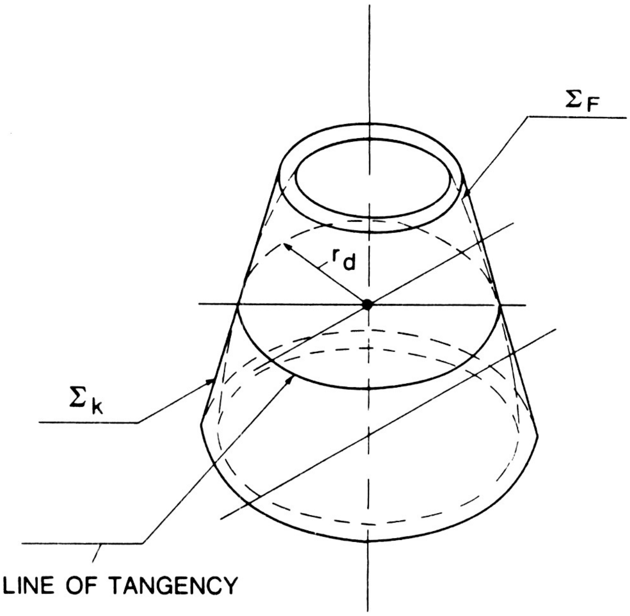

Figure 6. - Generating surfaces for geometry II.

Because of elasticity of gear surfaces, their contact under a load is spread over an area (fig. 9) which, when projected on the tangent plane, is an ellipse. Figure 10 shows how the bearing contact is formed for gears with geometry I (fig. 10(a)) and for gears with geometry II (fig. 10(b)). The location of the bearing contact on the tooth surface depends on the direction of motion of the elliptical spot over the tooth surface.

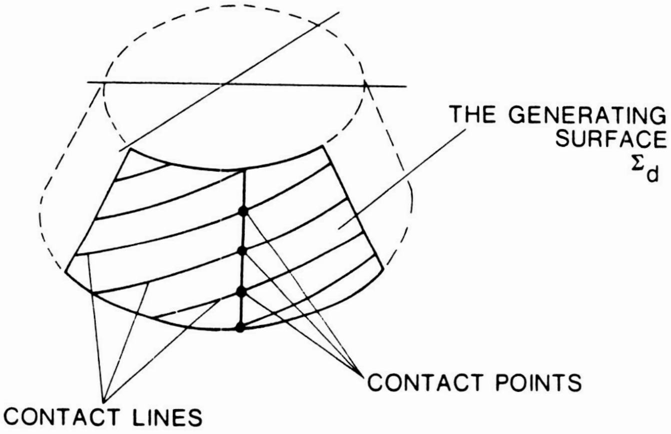

Figure 7. - Contact lines and contact points on generating surface Σ_d.

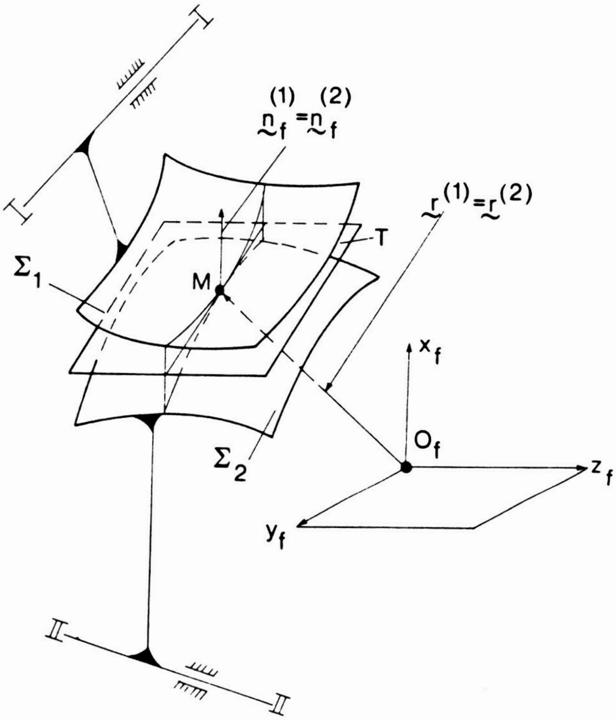

Figure 8. - Gear tooth surfaces at contact.

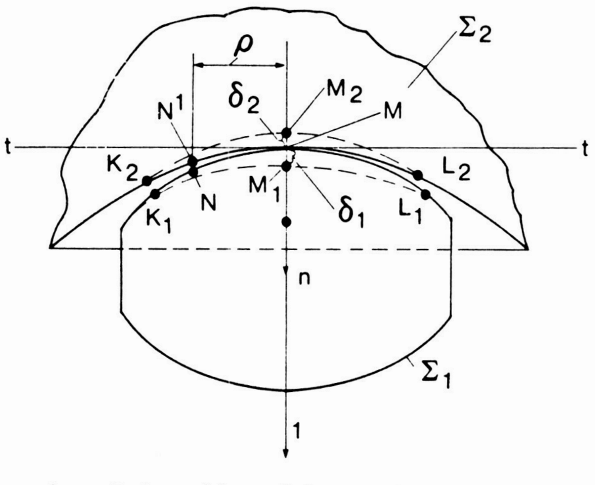

Figure 9. - Deformation of two contacting surfaces.

Method of Calculation of Dynamic Capacity and Surface Fatigue Life of Spiral Bevel Gears

In reference 1 a method of adapting the Lundberg-Palmgren method of life analysis for rolling-element bearings was applied to spur and helical gears. The method has also been applied to life analysis of traction drives (ref. 11). An update of the method applied to spur gears, with applications for various gearing arrangements, is presented in another paper in this symposium.

In the life analysis theory the important parameters are number of stress cycles, η, magnitude of critical stress, τ, amount of stressed volume, V, and depth below the surface at which the critical stress occurs, z. For spiral bevel gears, the stressed volume is taken as

$$V \propto wzl \tag{1}$$

where l is the length of the contact path which is traversed during one tooth mesh cycle and the semi-width of the contact path is designated w.

The probability of survival, S, for a tooth contact is given by the following expression:

$$\log\frac{1}{S} \propto \frac{\tau^c \eta^e V}{z^h} \tag{2}$$

This relation is consistent with experimental observations in the case of fatigue. The formula reflects the known fact that the more localized the stress is in the material (less stressed volume), the greater is the endurance. This is because, on a statistical basis, there is less likelihood of a fatigue nucleation site being coincident with a condition of high stress. Conversely, there is a greater probability of a crack forming in the zone of maximum critical stress, because the material is more rapidly cycled toward failure in that region. Hence the depth to the critical stress, as well as the magnitude of the stress is important, and with each stress cycle the probability of failure increases.

The number of stress cycles endured with 90 percent reliability is given by the following equation (ref. 11):

$$\eta = \left(\frac{Kz^h}{\tau^c V}\right)^{1/e} \tag{3}$$

Based on life testing of air-melted steel rolling-element bearings, the following values are valid for equation (3): $K = 1.43 \times 10^{95}$ (SI units), 3.58×10^{56} (English units); $h = 7/3$; $c = 31/3$; and $e = 10/9$ (point contact), 3/2 (line contact) (ref. 11).

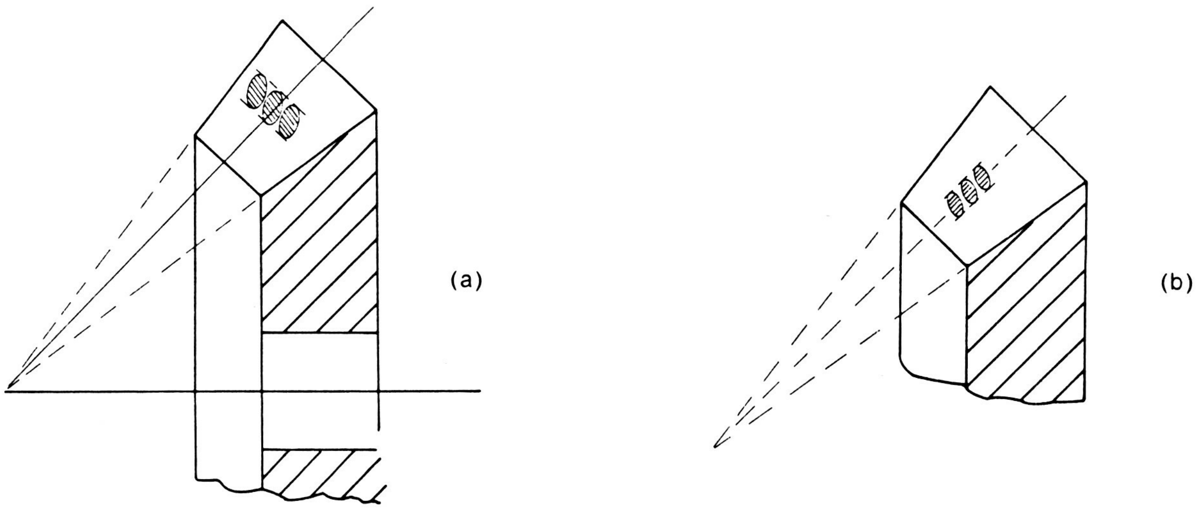

Figure 10. - Formation of bearing contact.

From the probability theory the life, L, of a gear with N teeth then is obtained by the equation

$$\left(\frac{1}{L}\right)^e = N\left(\frac{1}{\eta}\right)^e \tag{4}$$

The foregoing has been a brief summary of how the gear life analysis originally presented in reference 10 may be applied to spiral-bevel gears. All of the approximations, service life factors and lubricant-condition-related life-modifying factors that pertain to spur and helical gears will also have counterpart effects for spiral-bevel gears. These factors are discussed in reference 11.

Gear Train Precision

Angles of rotation φ_2 and φ_1 of a pair of gears are related by a linear function only for an ideal train. The difference

$$\varphi_2(\varphi_1) - \varphi_2^o(\varphi_1) = \Delta\varphi_2(\varphi_1) \tag{5}$$

represents a function of kinematical errors induced by errors of manufacturing and assembly. Here, $\varphi_2^o(\varphi_1)$ is the theoretical function, and $\varphi_2(\varphi_1)$ is the real function.

The function $\Delta\varphi_2(\varphi_1)$ of kinematical errors may be determined in the following two ways:

The first method is based on the investigation of the meshing of gear surfaces generated and assembled with some errors. The basic principle of such an investigation is the requirement of equality of radii vectors and unit normals of contacting surfaces (fig. 8). The determination of gear-train kinematical errors with such a method is a computer problem.

The second method is based on the following suggestions (fig. 11): Suppose that, because of errors of manufacturing and assembly, the expected contact points $M^{(1)}$ and $M^{(2)}$ do not coincide with each other and that between surfaces Σ_1 and Σ_2 there occurs clearance or interference. To bring both surfaces into contact, it is necessary and sufficient to rotate the driven gear 2 about the axis II-II by some small angle $\Delta\varphi_2$, the magnitude of which depends on the magnitude of clearance or

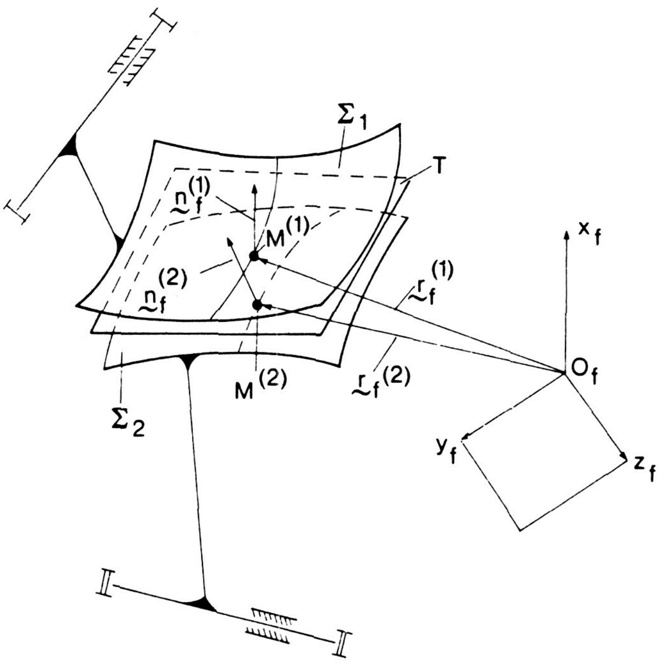

Figure 11. - Tooth surfaces with clearance induced by errors.

interference induced by errors of manufacturing and assembly. Equations relating kinematical errors with errors of manufacturing and assembly have been developed by Litvin (refs. 4 and 5).

Figure 12 shows kinematical errors $\Delta\varphi_2(\varphi_1)$ represented by equation (5). Figure 13 shows two types of the function $\Delta\varphi_2(\varphi_1)$. The first one (fig. 13(a)) corresponds to the case when the gear axis does not coincide with the axis of rotation and rotates about it in the process of meshing. The typical example of such errors is the gear eccentricity. The second type of kinematical errors of a train with spiral-bevel gears and hypoid gears is the result of the approximate way of gear generation (fig. 13(b)).

Figure 14 shows a case when a gear axis, z_1, forms an angle $\Delta\delta$ with the axis of rotation, z, and the shortest distance between z_1 and z is the rotated vector $\Delta\mathbf{e}$. With $\Delta\delta = 0$ the vector $\Delta\mathbf{e}$ represents the vector of gear eccentricity.

Figure 15 shows two spur involute gears with vectors of eccentricity $\Delta\mathbf{e}_1$ and $\Delta\mathbf{e}_2$. Gear axis of rotation are $O^{(1)}$ amd $O^{(2)}$, geometric centers of gears are O_1 and O_2. These centers rotate about $O^{(1)}$ and $O^{(2)}$ as shown in figure 16. The eccentricity of a spur gear exerts a harmonic function (fig. 17) of kinematical errors $\Delta\theta_1(\varphi_i)$, the period of which coincides with the period of a complete revolution of the considered gear. The distribution of this function in positive and negative areas depends on the location of the vector eccentricity.

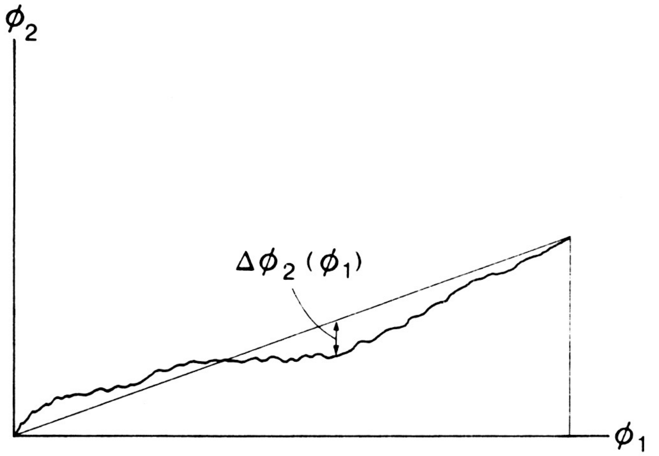

Figure 12. - Kinematic error functions.

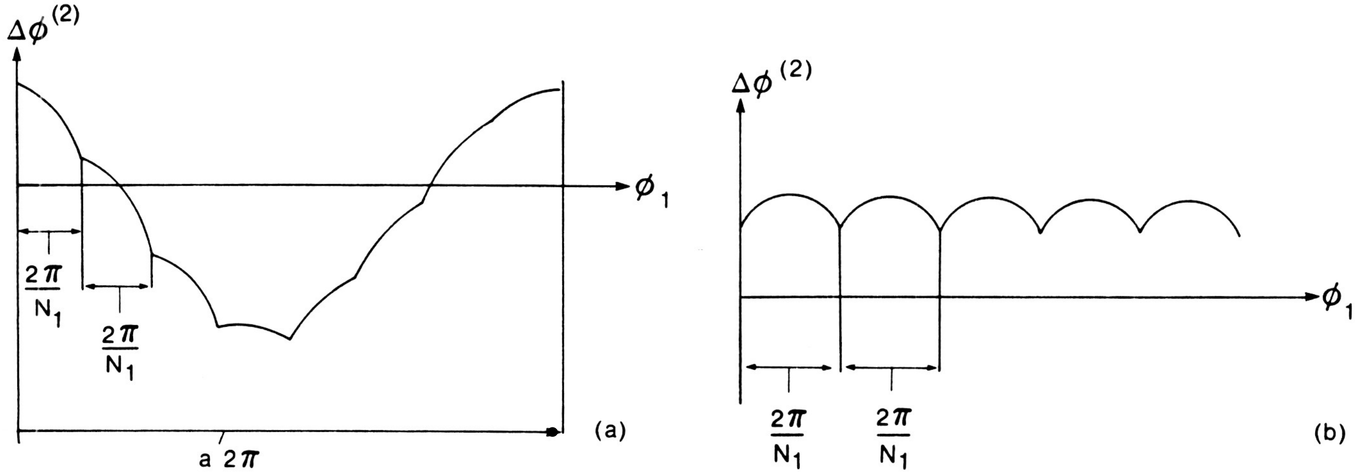

Figure 13. - Two types of kinematic functions.

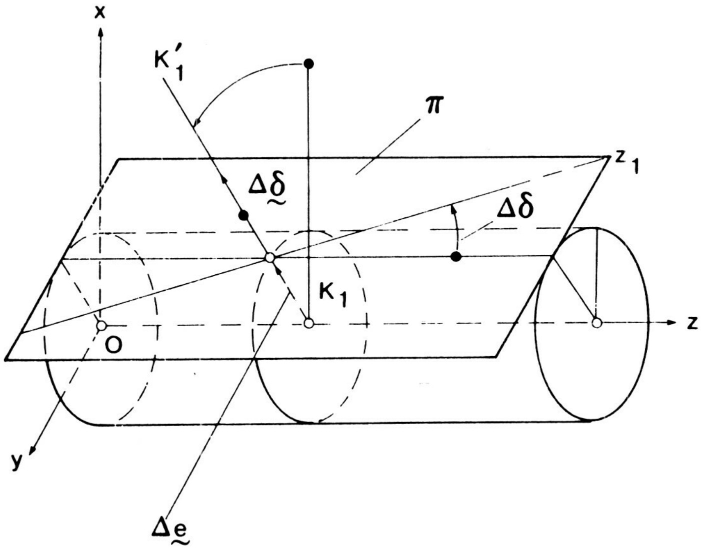

Figure 14. - Crossing of gear axis and rotation axis.

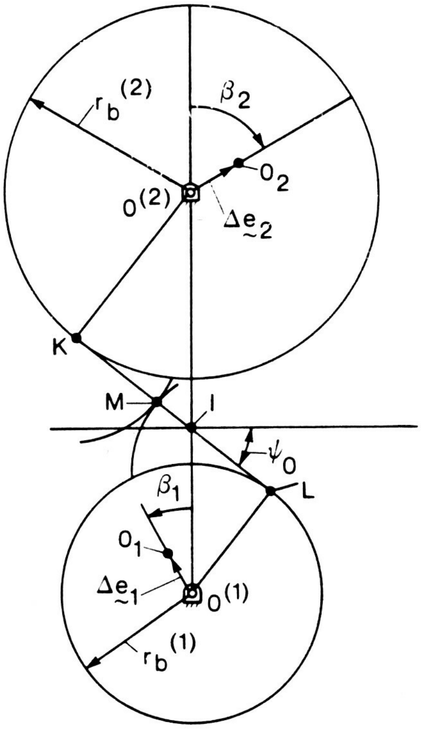

Figure 15. - Eccentricity of spur gears.

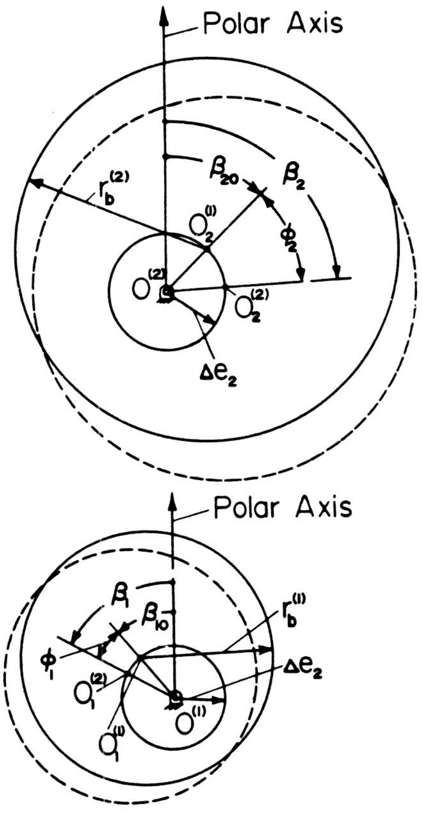

Figure 16. - Eccentric base circles.

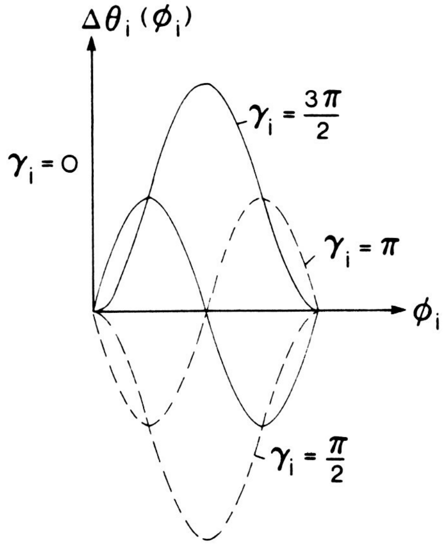

Figure 17. - Distribution of kinematic errors by eccentricity.

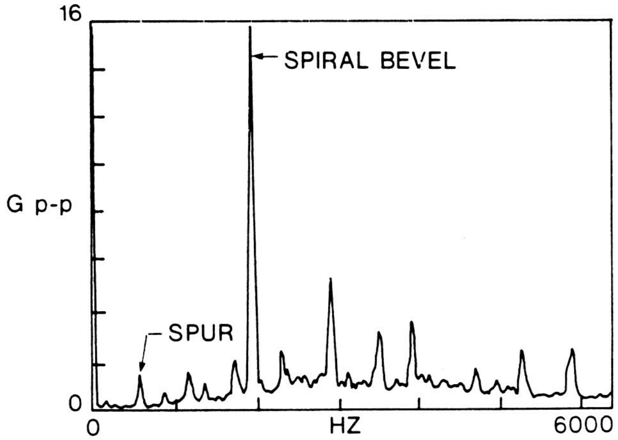

Figure 18. - Baseband frequency spectrum showing spiral bevel amplitude compared with spur.

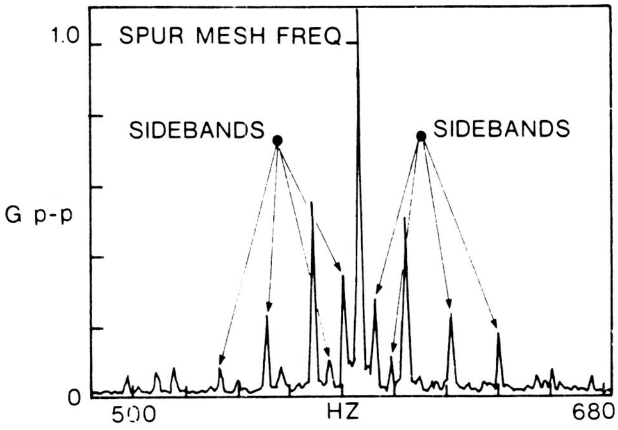

Figure 19. - Narrowband frequency spectrum showing sidebands around the spur mesh frequency.

Gear Train Vibration and Noise Measurement

To illustrate the principles discussed on the subject of gear-train precision, figures 18 and 19 are used. These figures show some frequency spectrum measurements made on a helicopter transmission running in a test stand (ref. 12). The transmission had a spiral-bevel input stage with 19 teeth on the pinion and 71 teeth on the gear. The pinion was turning at 6200 rpm and the output shaft at 355.5 rpm. The output stage was a spur planetary arrangement with a 27-tooth sun, 3 planet gears, each with 35 teeth, and a 99-tooth ring gear which was splined to the transmission housing. An accelerometer was mounted on the case immediately outside the spline.

Figure 18 shows a broadband frequency spectrum measurement of the vibration signal. The spur mesh frequency was 583 Hz, and the spiral bevel mesh frequency was 1963 Hz. The spiral bevel vibration signature was much stronger than the spur signature. This indicates that the meshing accuracy according to figure 13(b) was better for the spur mesh than for the spiral-bevel mesh. There are also other peaks in the spectrum at multiples of the fundamental frequencies of 1963 and 583 Hz. These other peaks are the higher harmonics due to the noise and vibration pulsations as the teeth mesh being different from the pure sinusoidal shape, as shown in figure 17.

Figure 19 shows an expanded region of the autospectrum plot given in figure 18. This figure shows many peaks which are symmetrically located about the spur gear mesh fundamental frequency peak at 583 Hz. These peaks locate the sideband frequencies which are due to sources of modulation in the time-dependent vibration waveform. Each source of modulation may produce one pair of sidebands if it is a harmonic modulator. If nonharmonic, the sidebands will repeat many times, as is the case in figure 19.

In this particular example, there are three major causes of modulation: (1) the planet gears passing the stationary accelerometer at approximately 18 Hz; (2) the planet gears rotational speed of 16 Hz; and (3) the planet carrier turning at the output shaft speed of 6 Hz. The misalinements and eccentricities associated with the rotational frequencies of the mentioned gear components cause these modulation sidebands to appear, as discussed in the previous section.

Conclusions

Two types of spiral-bevel geometry for a simplified study and investigation of such gears were described. The line of action and bearing contact for gears of both types of geometry were determined. A method for calculating the expected service life for pitting fatigue of the spiral-bevel gear teeth was given.

Two methods for the determination of kinematical errors induced by errors of manufacturing and assembly were proposed. The first is an exact computerized method, the second is an approximate one but one which allowed the analytical relations between source errors and resulting kinematical errors to be written. Results of noise and vibration measurements on a helicopter transmission were shown to illustrate the principles contained in the theory of kinematical errors.

References

1. Coy, J. J.; Townsend, D. P.; and Zaretsky, E. V.: Dynamic Capacity and Surface Fatigue Life for Spur and Helical Gears. J. Lubr. Technol., vol. 98, no. 2, April 1976, pp. 267-276.
2. Baxter, M.: Second-Order Surface Generation. Ind. Math., vol. 23, pt. 2, 1973, pp. 85-106.
3. Baxter, M.: Effect of Misalignment on Tooth Action of Bevel and Hypoid Gears. ASME Paper No. 61-MD-20.
4. Litvin, F.: Theory of Gearing, 2nd. Ed., Nauka, 1968 (in Russian).
5. Litvin, F.: Die Beziehungen zwishen den Krümmungen der Zahnoberflächen bei räumlichen Verzahnungen. ZAMM, 49 (1969), Heft 11, Seite 685-690.
6. Litvin, F.: The Synthesis of Approximate Meshing for Spatial Gears. J. Mechanisms, vol. 4, 1969, Pergamon Press, pp. 187-191.
7. Litvin, F.: An Analysis of Undercut Conditions and of Appearance of Contact Lines Envelope Conditions of Gears. J. Mech. Des., July 1978, pp. 423-432.
8. Litvin, F.; and Gutman, Ye.: Methods of Synthesis and Analysis for Hypoid Gear Drives of "Formate" and "Helixform," Pts. 1-3, J. Mech. Des., vol. 103, Jan. 1981, pp. 83-113.
9. Litvin, F.; and Gutman, Ye.: A Method of Local Synthesis of Gears Grounded on the Connections Between the Principal and Geodetic Curvatures of Surfaces. J. Mech. Des., vol. 103, 1981, pp. 114-125.
10. Wildhaber, E.: Surface Curvature—A Tool for Engineers. Ind. Math., vol. 5, 1954, pp. 31-116.
11. Coy, J. J.; Rohn, D. A.; and Loewenthal, S. H.: Life Analysis of Multiroller Planetary Traction Drive. NASA TP-1710, April 1981.
12. Townsend, D. P.; Coy, J. J.; and Hatvani, B. R.: OH-58 Helicopter Transmission Failure Analysis. NASA TM X-71867, Jan. 1976.

A Computer Solution for the Dynamic Load, Lubricant Film Thickness, and Surface Temperatures in Spiral-Bevel Gears[*]

H. C. Chao,[†] M. Baxter,[‡] and H. S. Cheng[§]

Spiral-bevel gears, found in many machine tools, automobile rear-axle drives, and helicopter transmissions, are important elements for transmitting power. However, the basic mechanisms which govern the major failure modes of spiral gears are still not fully understood. Because of the complicated geometry of spiral-bevel gears, the analyses are considerably more difficult than those conducted earlier for spur and helical gears. In military applications, such as the transmissions used in V/STOL aircraft, gears are often designed under conditions very close to the failure limits for maximum power density. A thorough understanding of spiral-bevel gears under critical operations is urgently needed to prevent premature failure.

Gear failures usually fall into two categories, structural failures, which include flexure fatigue, tooth breakage, case crushing, and lubrication-related failures, which include wear, surface pitting, and scuffing. Among these types of failure modes, lubrication-related failures are much more difficult to predict since the basic mechanisms are still not fully understood. Current methods used for predicting gear pitting and scuffing are mainly empirical and are not completely reliable. Recent failure tests of gears and rollers strongly suggest that surface pitting as well as scuffing are critically influenced by lubricant film thickness and surface temperature in the gear teeth contact. To develop improved methods for failure prediction, it is important to develop accurate tools to determine the film thickness and surface temperature.

In this paper a computer method is first described for determining the dynamic load between spiral-bevel pinion and gear teeth contact along the path of contact. The dynamic load analysis is necessary because it governs both the surface temperature and film thickness. Computer methods for determining the surface temperature and film thickness are then presented along with some results obtained for a pair of typical spiral-bevel gears.

Symbols

$\{D\}$	displacement column vector for pinion or gear in x, y, z coordinates, m or rad (ft or rad)
$\{D'\}$	displacement column vector for pinion or gear in x', y', z' coordinates, m or rad (ft or rad)
$[DC_{ji}]$	elastic compliance matrix, m/N (ft/lb)
$[DK_j]$	bearing stiffness matrix, N/m (lb/ft)
$\mathbf{F}_c$	teeth contact force, N (lb)
$\mathbf{F}_r$	bearing force, N (lb)
$I_{x'},I_{y'},I_{z'}$	polar moment of inertia about x', y', z' axes, kg·m^2 (slug·ft^2)
$\mathbf{i}',\mathbf{j}',\mathbf{k}'$	unit vectors along the x', y', z' axes

---

[*] Work done under NASA Lewis contract NSG-3143.

[†] Garrett Turbine and Engine Co.

[‡] Consultant, Gear Technology.

[§] Northwestern University.

m	mass of pinion or gear shaft, kg (slug)
$\mathbf{r}_c$	position vector of the teeth contact point with respect to the mass center, m (ft)
$\mathbf{r}_r$	position vector of the bearing supports with respect to the mass center, m (ft)
$T_{\text{in}}, T_{\text{out}}$	average input torque, average output torque, N·m (ft·lb)
X, Y, Z	fixed coordinates with origin at the intersection of two shafts
x, y, z	fixed coordinates with origin at the mass center of the pinion or gear
x', y', z'	moving coordinates along the principal axes of inertia of pinion or gear
x'_c, y'_c, z'_c	displacements of mass center of pinion or gear, m (ft)
$\theta_{x'}, \theta_{y'}, \theta_{z'}$	angular displacements of pinion or gear, rad
ω	angular velocity of pinion or gear shaft, rad/sec
Subscripts:	
g	gear shaft
p	pinion shaft

Dynamic Load

Equations of Motion

Figure 1 shows the model used for deriving the equations of motion to simulate the steady-state, periodic motion of both pinion and gear as well as the tooth load during a typical cycle during which a pair of teeth traverse through the zone of action from point A to point C. In developing the equations of motion, the pinion and gear are assumed to be rigid bodies each having 6 degrees of freedom. The supporting radial and thrust bearings are assumed to be flexible with known spring stiffnesses. At the contact of each mesh, the teeth are assumed to be connected by a linear spring, which is oriented normal to the contact point and has a stiffness to be determined separately by a finite-element model.

Based on Newtonian mechanics, it is shown (ref. 1) that the equations governing the pinion motion can be expressed in a moving coordinate axes x'_p, y'_p, z'_p, which are instantaneous principal axes of inertia of the pinion. However, the pinion is not fixed in the axes x'_p, y'_p, z'_p, but rotates about the y'_p axis with a nominal angular velocity ω_p. The two vectorial equations of motion for the pinion are

$$\sum_{i=1}^{M} \mathbf{F}_{rpi} + \sum_{i=1}^{N} \mathbf{F}_{cpi} = m_p(\ddot{x}'_{cp}\mathbf{i}'_p + \ddot{y}'_{cp}\mathbf{j}'_p + \ddot{z}'_{cp}\mathbf{k}'_p) \tag{1}$$

$$\sum_{i=1}^{M} \mathbf{r}_{rpi} \times \mathbf{F}_{rpi} + \sum_{i=1}^{N} \mathbf{r}_{cpi} \times \mathbf{F}_{cpi} + \mathbf{T}_{\text{in}} = (I_{x'p}\ddot{\theta}_{x'p} - I_{y'p}\omega_p\dot{\theta}_{z'p})\mathbf{i}'_p + I_{y'p}\ddot{\theta}_{y'p}\mathbf{j}'_p + (I_{z'p}\ddot{\theta}_{z'p} + I_{y'p}\omega_p\dot{\theta}_{x'p})\mathbf{k}'_p \tag{2}$$

where M is the total number of bearing forces acting on the pinion shaft and N is the total number of contact forces.

Similarly, the equations of motion for the gear can be expressed in the coordinate axes x'_g, y'_g, z'_g, and the gear rotates about the x'_g axis with a nominal angular velocity, ω_g. The two vectorial equations for the gear appear as

$$\sum_{i=1}^{M} \mathbf{F}_{rgi} + \sum_{i=1}^{N} \mathbf{F}_{cgi} = m_g(\ddot{x}'_{cg}\mathbf{i}'_g + \ddot{y}'_{cg}\mathbf{j}'_g + \ddot{z}'_{cg}\mathbf{k}'_g) \tag{3}$$

$$[m]\begin{Bmatrix}\{\ddot{D}'\}_g\\ \\ \{\ddot{D}'\}_p\end{Bmatrix}+[C]\begin{Bmatrix}\{\dot{D}'\}_g\\ \\ \{\dot{D}'\}_p\end{Bmatrix}+[K]\begin{Bmatrix}\{D'\}_g\\ \\ \{D'\}_p\end{Bmatrix}=\{R\} \tag{7}$$

The details of matrix $[m]$, $[c]$, $[k]$, and $\{R\}$ can be found in reference 2.

It was also found that the rotational equations governing the perturbed gear rotation $\theta'_{x'g}$ and the perturbed pinion rotation $\theta'_{y'p}$ can be combined into one equation to solve for the relative angles θ'_{yp} and θ'_{xg}. Thus, the reduced system becomes a set of 11 equations which are solved by Runge-Kutta procedure for the displacements of pinion and gear mass center and their small angular rotaions.

In implementing these equations, the information needed includes

(1) The tooth contact position as a function of the relative rigid body displacements of the two shafts

(2) The direction of normal vector at the contact point

(3) The combined stiffness of the teeth at the contact point.

The teeth contact position and the direction of the contacting normal vector are obtained from a computer code (ref. 3). Because of the geometric complexity of spiral-bevel gears, calculations of combined teeth stiffness are not as simple as those shown in reference 4 for spur gears. For this study, a large-scale finite-element program is used to calculate the deformation due to a unit load at various contact points in the zone of action for a given set of spiral-bevel gears.

Tooth Deflection

For most gears the contact ratio is greater than one, and the load is, in general, not equally shared among the pairs of teeth in contact because the system is a statically indeterminate case. Therefore, one must consider the tooth deflection under the load for each pair in order to determine the load sharing characteristics among the pairs.

Because of the complexity of the spiral-bevel gear geometry, there is no simplified method currently available to calculate the tooth deflection. In order to investigate the system response, shaft deformation must also be included in the calculation of tooth deflection. Therefore, it is more difficult to calculate the tooth deflection by some simple equations. A numerical solution using finite-element method is used to overcome these difficulties.

Some of the recent work (refs. 5 and 6) has proven that the finite-element method yields better results in determining tooth deflection. However, most of this work dealt with two-dimensional problems and did not include the whole gear body. In the present work the spiral-bevel geometry necessitates the use of a three-dimensional, finite-element code. Figure 2 shows a typical eight-node, solid-element grid pattern for a typical spiral-bevel gear and pinion with three adjacent teeth attached to the gear wheel and shaft. Figure 3 shows a central tooth and its attached ring element of gear. Figure 4 shows parts of a gear shaft and gear wheel. Figure 5 shows whole ring elements with three adjacent teeth of pinion. Figure 6 shows the elements of pinion shaft. Only the central tooth is loaded to calculate the deflection. There are 941 nodes, 562 elements for the gear model and 1029 nodes, 584 elements for the pinion model. Using these grids, one can readily compute the deflection δ under a load P applied at any grid point on the tooth surface. For this analysis the MARC–CDC program was used; the boundaries are considered to be fixed for all the points connected to the thrust bearing to eliminate rigid body displacement; and the boundary nodes connected to the radial bearing were allowed to move in the direction of the rotational axis.

The stiffness at grid point i is defined as

$$KS_{gi}=\frac{P}{\delta_{gi}}$$

$$KS_{pi}=\frac{P}{\delta_{pi}}$$

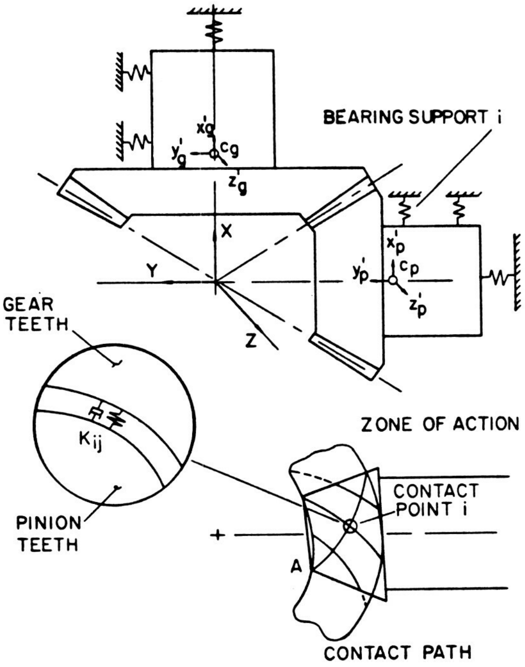

Figure 1. - Geometry and mathematical model of spiral-bevel gears.

$$\sum_{i=1}^{M} \mathbf{r}_{rgi} \times \mathbf{F}_{rgi} + \sum_{i=1}^{N} \mathbf{r}_{cgi} \times \mathbf{F}_{cgi} + \mathbf{T}_{\text{out}} = I_{x'g}\dot{\theta}_{x'g}\mathbf{i}'_g$$

$$+ I_{y'g}\ddot{\theta}_{y'g} + I_{x'g}\omega_g\dot{\theta}_{z'g})\mathbf{j}'_g + (I_{z'g}\ddot{\theta}_{z'g} + I_{x'g}\omega_g\dot{\theta}_{y'g})\mathbf{k}'_g \qquad (4)$$

In these four equations of motion, $\mathbf{F}_{rpi}$ and $\mathbf{F}_{rqi}$ are the bearing reaction forces for the pinion and gear. These can be expressed directly as the product of the stiffness and the displacement vectors in matrix form as

$$\{F_{rj}\}_g = -[DK_j]_g\{D\}_g$$

$$\{F_{rj}\}_p = -[DK_j]_p\{D\}_p \qquad (5)$$

The tooth contact forces $\mathbf{F}_{cpi}$ and $\mathbf{F}_{cqi}$ at the contact point are equal and opposite forces, and $\mathbf{F}_{cqi}$ in matrix form can be expressed in terms of the combined teeth elastic compliance matrix $[DC_{ij}]$ and the displacement vectors $\{D\}_p$ and $\{D\}_g$ as

$$\{F_{ci}\}_g = -([DC_{ji}]_g + [DC_{ji}]_p)^{-1}([DG_i]_g\{D\}_g + [DG_i]_p\{D\}_p) \qquad (6)$$

Substituting equations (5) and (6) into equations (1) to (4), one obtains a set of 12 equations, which can be put in the following matrix form:

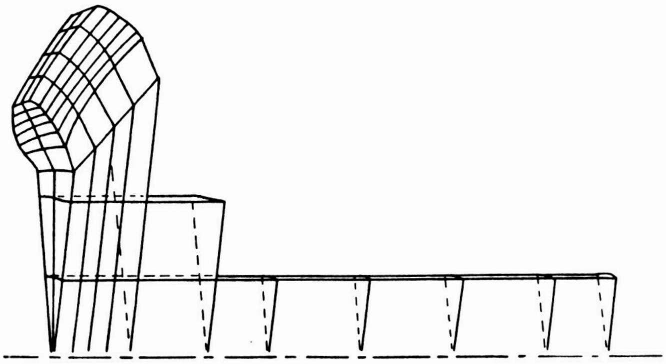

Figure 2. - Typical section of finite elements of gear segment.

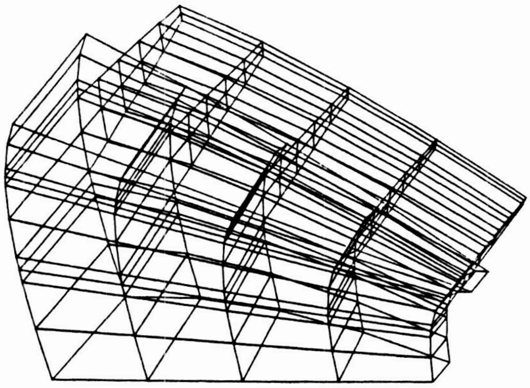

Figure 3. - Center tooth elements and attached ring elements of gear.

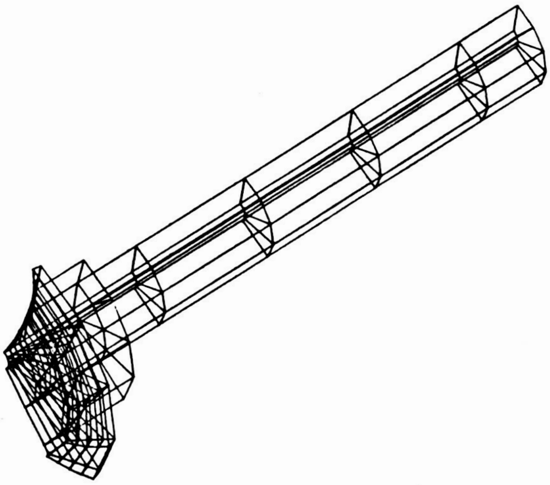

Figure 4. - Elements for segment of shaft and wheel.

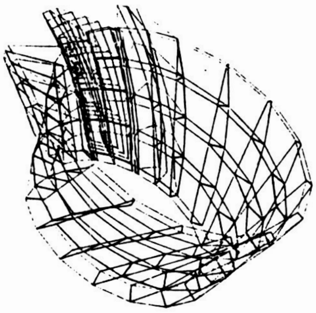

Figure 5. - Elements of three pinion teeth and rim.

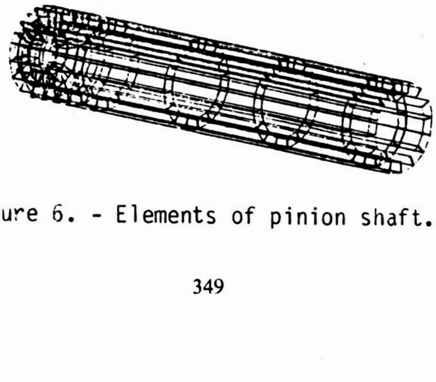

Figure 6. - Elements of pinion shaft.

The stiffness of a point other than a grid point on the tooth surface can be calculated by the interpolation method. The combined stiffness at the contact point is found to be

$$KS = \frac{KS_g \cdot KS_p}{KS_g + KS_p}$$

Results of Dynamic Load

A series of solutions were obtained to simulate the dynamic response of a set of spiral-bevel gears currently being tested at NASA Lewis. The data for this gearset and the lubricant data are listed in table I. Effects studied include the running speed, shaft misalinement, and system damping. These results are presented in this section. The dynamic response is expressed by a dynamic load factor defined as the ratio of the maximum dynamic load along the contact path to the average static load. This factor is plotted as a function of speed with different damping ratios and contact ratios.

TABLE I. – GEAR AND LUBRICANT DATA

Gear data:	
Number of teeth:	
Gear	36
Pinion	12
Pitch angle:	
Gear	71°34′
Pinion	18°26′
Shaft angle, deg	90
Spiral angle, deg	35
Diametral pitch	5.14
Standard operating conditions:	
Gear rpm	5000
Pinion rpm	15 000
Load at pitch point, N (lb)	11 800 (2660)
Ambient temperature, °C (°F)	37.8 (100)
Geometry dimensions (see fig. 25), m (in.):	
DGG	0.1658 (6.527)
ROG	0.07620 (3.0)
RIG	0.04336 (1.707)
RZG	0.1964 (7.733)
DGP	0.2515 (9.901)
ROP	0.07620 (3.0)
RIP	0.09311 (3.6656)
RZP	0.1987 (7.824)
Gear material data:	
Material	steel
Density, g/cm^3 (lb/in^3)	7.81 (0.282)
Thermal conductivity at 311 K (100° F), W/mK (Btu/sec·in·°F)	46.7 (0.000625)
Young's modulus, GPa (psi)	207 (30 000 000)
Poisson ratio	0.3
Surface convectivity, W/m^{2}K (Btu/sec·in^2·°F):	
Oil jet	397 (0.000135)
Oil/air mist	19.8 (0.00000765)
Air	3.97 (0.00000135)
Lubricant data:	
Material	superrefined, naphthenic, mineral oil
Dynamic viscosity at 311 K (100° F), cp (lb·sec/in^2)	64.7 (0.00000938)
Density at 311 K (100° F), g/cm^3 (lb/in^3)	0.61 (0.022)
Thermal conductivity at 311 K (100° F), W/mK (Btu/sec·in·°F)	0.125 (0.00000168)
Pressure viscosity coefficient, α, m^2/MN (in^{2}lb)	0.023 (0.00016)
Temperature-viscosity coefficient, β, K (°R)	3890 (7000)
Viscosity-pressure temperature relation	$\mu = \mu_o \exp\{\alpha p + \beta[(1/T) - (1/T_0)]\}$

Dynamic Load Variation

For constant input torque the load on the contact point of the two meshing teeth along the path of contact is not constant; this load variation is mainly caused by the following factors:

(1) The variation of stiffness along the contact path
(2) The transition from single pair of contacts to double and from double to single
(3) The effective radius not constant along the contact path.

Figure 7 shows the variation of stiffness for the transition of contacts.

The main excitation to the gear system comes from the periodical change in teeth stiffness due to the alternating engagement of single and double pairs of teeth. The frequency of this excitation force expressed as a meshing frequency depends on the operating speed. Therefore, it dominates the resulting mode of vibration. Figures 8 to 11 show dynamic load variation at four different speeds in the case of central contact; that is, the contact path located centrally between the toe and heel of the tooth.

Since there are 11 degrees of freedom in the system, 11 resonating frequencies of the system should exist. In the low-speed region where the excitation frequency from the change of stiffness is much lower than all resonating frequencies, the dynamic load response along the path of contact is somewhat like static load superimposed by an oscillatory load due to the system's resonating frequency.

When the speeds are near the resonance region (fig. 8), the dynamic load response becomes very severe (figs. 9 and 10). The maximum dynamic load is much higher than the static load, which is the

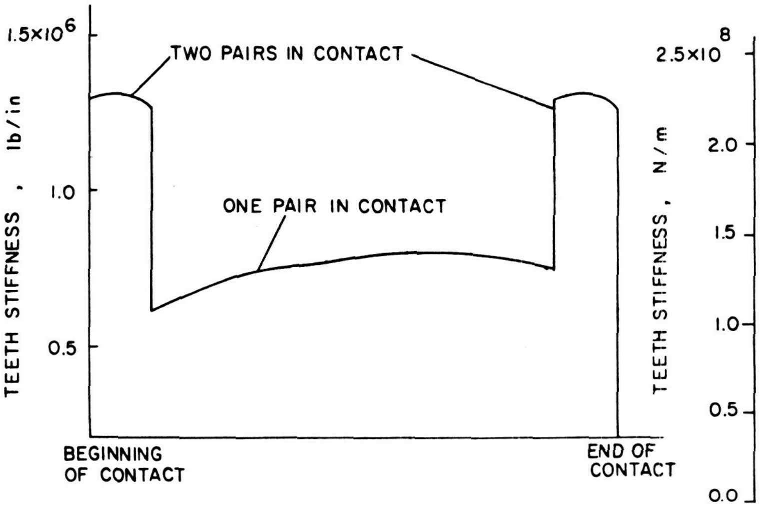

Figure 7. - Stiffness variation along contact path.

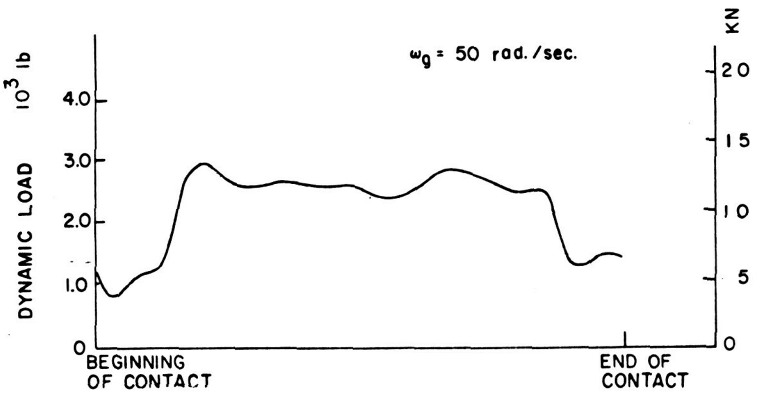

Figure 8. - Dynamic load variation along contact path. Central contact position, ω_g = 50 rad/sec.

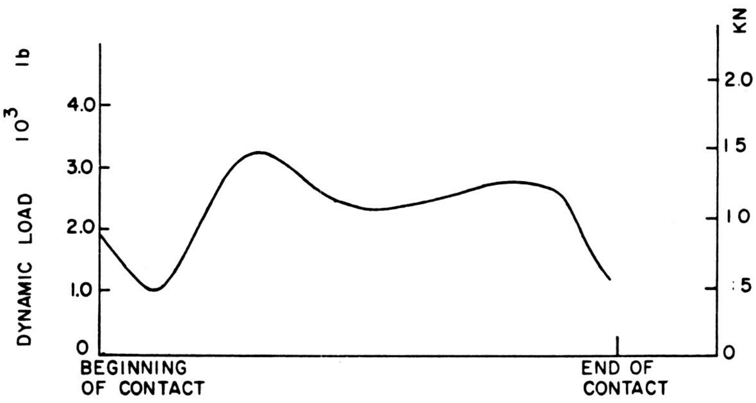

Figure 9. - Dynamic load variation along contact path. Central contact position, ω_g = 150 rad/sec.

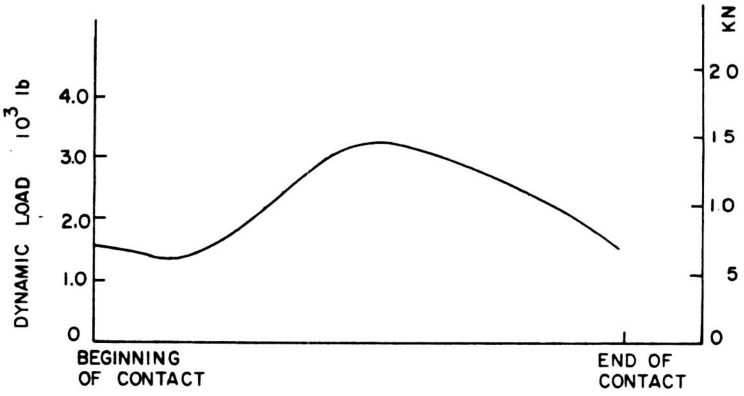

Figure 10. - Dynamic load variation along contact path. Central contact position, ω_g = 300 rad/sec.

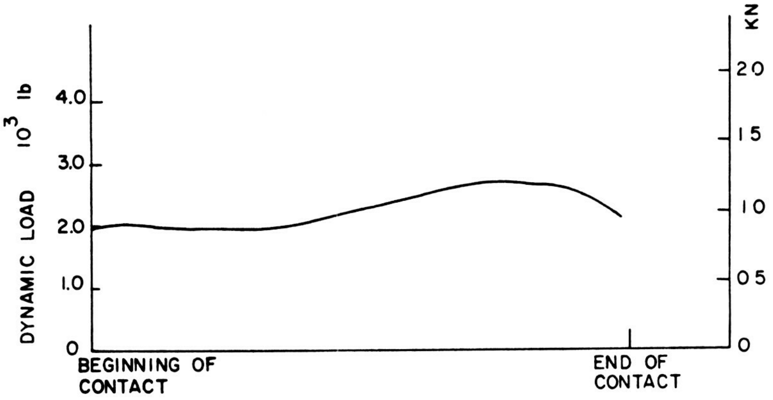

Figure 11. - Dynamic load variation along contact path. Central contact position, ω_g = 523 rad/sec.

case when overloading occurs. Sometimes the oscillation of dynamic load will make meshing teeth separate when the load becomes negative and thus will generate noise and surface fatigue.

As the speed increases beyond the zone of resonating frequencies, the dynamic load becomes smoother along the contact path, and the value is less than the static load (if the contact ratio is greater than one). The variation of dynamic load at this region is out of phase with the change of the teeth stiffness (fig. 11).

Effect of Shaft Misalinement

When the assembly errors are introduced in the system, the contact bearing will shift to either end of the tooth surface (ref. 7). Figure 12 shows the typical paths of central contact, toe contact, and heel contact. Usually the central contact is desired because it can tolerate more possible running position errors and avoid edge contact. The dynamic load response of toe and heel contact is shown in figures 13 and 14. The change of the contact bearing from center to either edge will also change the contact ratio of the system because the tooth surface is not a perfect involute along the profile direction and is mismatched along the lengthwise direction. In the current example the contact ratio for the toe contact is 1.26, the central contact, 1.16, and the heel contact, 1.0. In this case, if the contact bearing is moved farther toward the heel region, there would be no tooth contacts between the time when the previous tooth finishes the contact and the current tooth goes into the contact zone (discontinuity in tooth mesh). This situation would cause very large impact force which would generate noise and severe damages to the tooth surface. The effect of the tooth contact ratio on dynamic response is shown later.

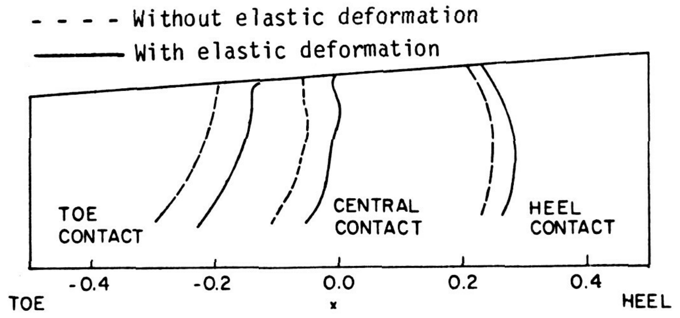

Figure 12. - Typical contact path for central, toe, and heel contact positions.

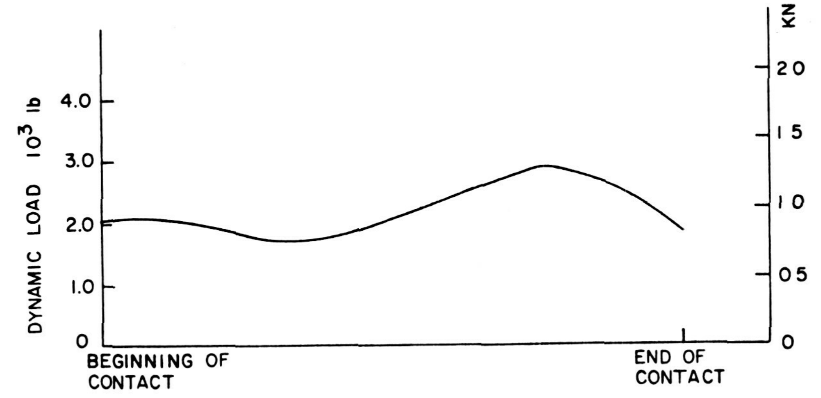

Figure 13. - Dynamic load variation along contact path. Toe contact position, ω_g = 523 rad/sec.

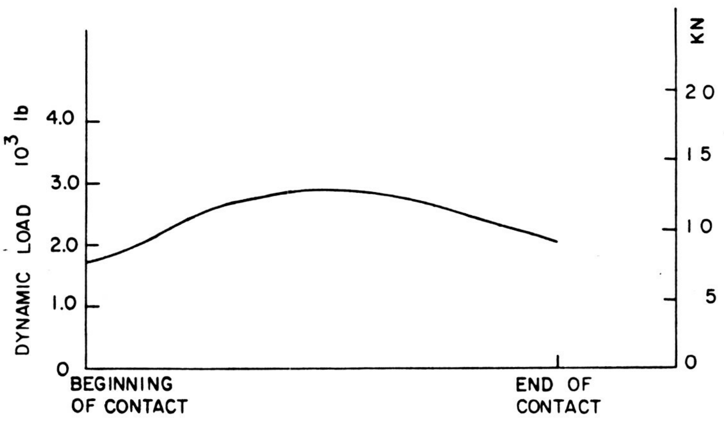

Figure 14. - Dynamic load variation along contact path. Heel contact position, ω_q = 523 rad/sec.

Contact Path Variation Due to Dynamic Response

In addition to showing the contact paths due to the assembly errors in the system in figure 12, the real contact path, not only due to the assembly errors but also to the running position errors induced by the dynamic responses, is plotted in the same figure. When this real contact path is compared with that caused by the assembly errors and running position errors induced by the average static elastic deformations, the deviation is found to be surprisingly small. One explanation of this small difference might be that the displacements changes due to the dynamic oscillation are small and that they do not produce a large change in contact path compared with those caused by the static displacements only. The closeness between these two contact paths suggests that one can use average static elastic deformation to calculate contact path, which can be used directly to solve for the dynamic load and lubrication problems without having to solve the dynamic load and contact path simultaneously using an iterative technique. The elimination of this iterative procedure greatly reduces the computation time.

Effect of Speed

Once the physical conditions of a gearset are determined, the dynamic response depends on the operating speed. For the system of 1 degree of freedom, such as spur gears, the maximum dynamic load occurs when the meshing frequency, which depends on the operating speed, is near the system natural frequency. Some peaks of dynamic load are caused by the varied meshing stiffness along the contact path, and they appear at meshing frequencies lower than the system natural frequency. The dynamic load factor, defined as the ratio of maximum dynamic load to the average static load, is plotted against the gear speed to illustrate the effect of speed in figure 15. Since there are 11 degrees of freedom in the spiral-bevel gear system, more peaks of dynamic load are expected.

The highest dynamic load appears to occur near the natural frequencies that correspond to the mode associated with a larger displacement in the motion along the line of action. The frequency marked ↑ in figure 15 shows the system natural frequency causing a larger displacement in the motion along the line of action, and the one marked ↓ shows the system natural frequency with a small displacement in that motion. It is clearly shown that the dynamic load factor at the frequency marked ↑ has a peak response and that the response at the natural frequency marked ↓ is not necessarily a peak.

Effect of Contact Ratio

The contact ratio is defined as the ratio of the duration for one tooth going through the whole contact zone to the duration of a periodic meshing cycle. It is believed that the load sharing characteristics caused by more than one tooth in contact will reduce the static load. The dynamic load factor due to the effect of contact ratio is shown in figure 16. It can be seen that the maximum

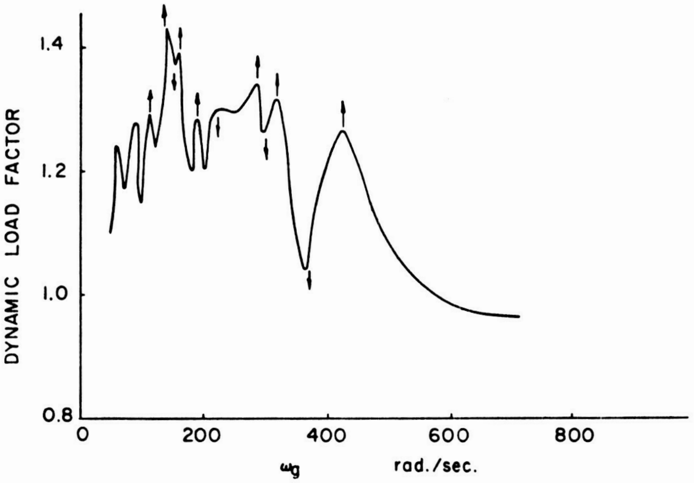

Figure 15. - Dynamic load factor versus gear speed. All damping coefficients, 2627 N·s/in (15 lb·s/in); contact ratio, 1.16.

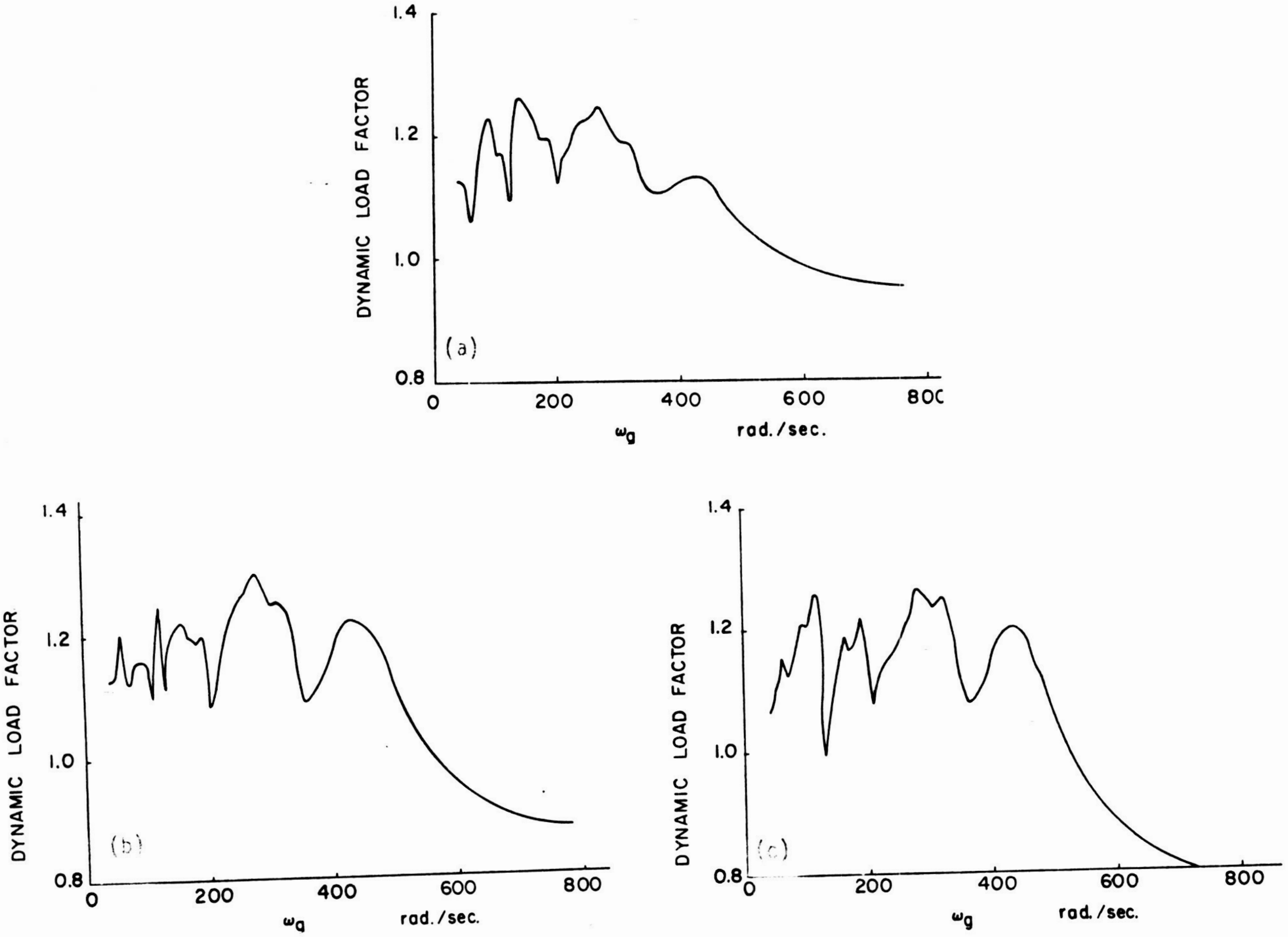

Figure 16. - Dynamic load factor versus gear speed. All damping coefficients, 4378 N·s/in (25 lb·s/in). (a) Contact ratio, 1.16; (b) contact ratio, 1.33; (c) contact ratio, 1.72.

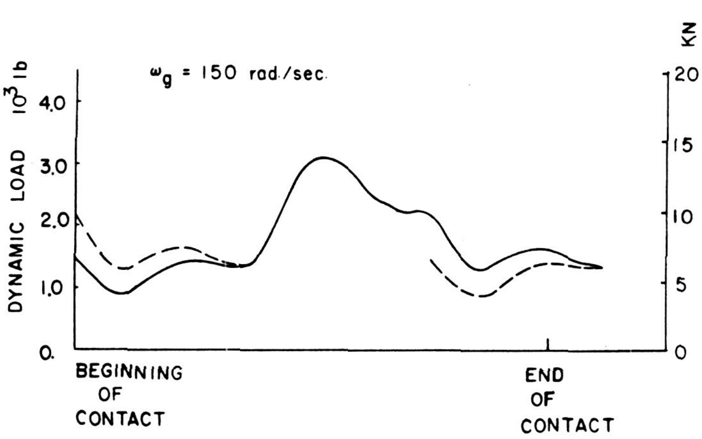

Figure 17. - Dynamic load variation along contact path. Damping coefficient, 4378 N•s/in (25 lb•s/in); contact ratio, 1.72.

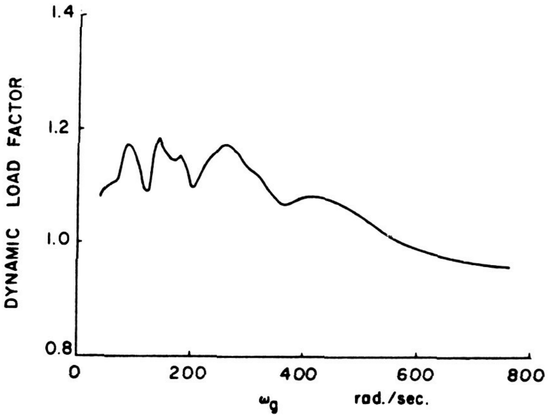

Figure 18. - Dynamic load factor versus gear speed. All damping coefficients, 6129 N•s/in (35 lb•s/in); contact ratio, 1.16.

dynamic load factor does not change much. However, the effect of contact ratio is significant in high-speed region, where the load is spread out averagely between meshing teeth path. A typical dynamic load variation with a high contact ratio along the contact path is shown in figure 17.

Effect of Damping

Since the damping forces are usually not known in the gear system, three arbitrary values are chosen for the damping coefficients: 2627, 4378, and 6129 N·sec/m (15, 25, and 35 lb·sec/m). These values are selected to give a range of nondimensional damping ratios corresponding to those commonly used in spur gears (0.1 to 0.2). The nondimensional damping ratios that correspond to the above three damping coefficients are 0.087, 0.14, and 0.203. The dynamic response for these damping cases can be observed from figures 15, 16(a), and 18. It is expected that the larger the damping force, the smaller the dynamic load factors will be in the resonance region. The large damping force will also level off the peak of dynamic load factor in the subresonance region, and there is no effect to the dynamic load factor due to damping force in the superresonance region.

Lubrication of Spiral-Bevel Gears

It is well accepted that the two major modes of gear failure, surface pitting and scuffing, are most strongly related to lubrication at the contact. Considerable gains in pitting life can be realized if the ratio of the lubricant film thickness to the surface roughness is increased. The knowledge of film thickness is believed to be essential for developing new analytical models for the prediction of surface durability for spur and helical, as well as spiral-bevel, gears. The variation of film thickness along the path of contact is mainly controlled by the local inlet lubricant viscosity, the local entrainment velocity, and the local contacting load. The local inlet lubricant viscosity, in turn, depends on the bulk surface temperature at the inlet of the contact. Since the bulk surface temperature is directly controlled by the sliding heat generated by the sliding tractive force which is, in turn, affected by the film thickness, the temperature and film thickness are mutually dependent and are solved simultaneously. The approach used in solving the simultaneous film thickness and bulk surface temperature is very similar to that used by Wang and Cheng (ref. 7) with the exception that the three-dimensional, spiral gear geometry necessitates the use of the point contact EHL theory for the film thickness and a three-dimensional, finite-element temperature code for the temperature influence coefficients, which are required for calculating the bulk surface temperature.

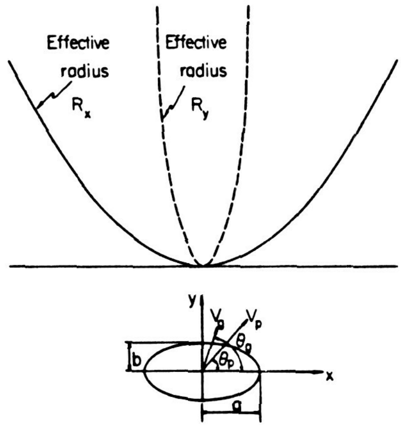

Figure 19. - Equivalent EHL point contact for spiral-bevel pinion and gear.

Lubricant Film Thickness

In determining the lubricant film thickness, the quasi-steady-state model is used, and the transient squeeze-film effect, which was included in a previous work for spur gears, is neglected in this film analysis for spiral-bevel gears. The neglecting of this squeeze-film effect is justified on the basis that it was shown by Wang and Cheng in spur gears to be a secondary effect.

The contact of a spiral-bevel gear and pinion set can be seen in figure 19, in which there is effectively a flat plane contact with a body, which is described by the difference of the neighboring surfaces between gear and pinion at contact point. This curved body has effective radii R_x and R_y along the principal axes, x and y, respectively. Under a load P, the surface near the flat plane will deform to an elliptical shape with semimajor axis a and semiminor axis b. The velocities of the pinion and gear at the contact point are V_p and V_g. The ellipticity parameter is defined as a/b. The minimum film thickness in the contact zone, following Hamrock and Dowson (ref. 8), can be related to Dowson-Higginson's line contact solution (ref. 9) by the equation

$$H_{\min} = H_{\min,l}\,(1.0 - 1.6\,e^{-0.62\,k}) \tag{10}$$

$$k = \frac{a}{b}$$

$$H_{\min} = \frac{h_{\min}}{R_x}$$

$$R_x = \frac{R_{x1}R_{x2}}{R_{x1} + R_{x2}}$$

$$u_{px} = V_p \cos \theta_p$$

$$u_{py} = V_p \sin \theta_p$$

$$u_{gx} = V_g \cos \theta_g$$

$$u_{gy} = V_g \sin \theta_g$$

$$u_x = \frac{U_{px} + U_{gx}}{2}$$

$$u_y = \frac{Y_{py} + U_{gy}}{2}$$

$$V = \sqrt{U_x^2 + U_y^2}$$

where

$H_{\min,l}$	dimensionless film thickness of Dowson-Higginson solution
V_p, V_g	velocity of pinion or gear tangent to contact plane
θ_p, θ_g	angle between pinion or gear velocity and y axis

The dimensional $h_{\min,l}$ can be expressed as

$$h_{\min,l} = 1.6\,\alpha^{0.6}\,(\eta_o V)^{0.7}\,E'^{\,0.03}\,\frac{R_x^{0.43}}{W^{0.13}} \tag{11}$$

where

α	pressure viscosity coefficient
η_o	viscosity taken at bulk surface temperature
W	effective line contact load per unit length
E'	$[(1 - \nu_1^2)/2E_1 + (1 - \nu_2^2)/2E_2]^{-1}$

It is important to note that η_o, W, k, and V are variables along the contact path. The V depends on the gear kinematics; a and b depend on the gear geometry; and η_o depends strongly on the local bulk surface temperature which is, in turn, influenced by the local film thickness through the frictional heating. Thus, the film thickness and the bulk surface temperature are interdependent and are solved as a coupled system.

Bulk Temperature

Before the gear system starts to operate, all elements are in ambient temperature. Then the temperature builds up as gears are running, due to the frictional heat generation. After a sufficient period of running, the gears reach a steady-state temperature, that is, the heat flux flowing into the body equals that flowing out of the body. At each revolution the tooth is subject to the same heating condition. Since the time period of each contact point in the contact zone is only a very small fraction of the period of revolution, the local temperature jump (flash temperature) is completely damped out before it enters the contact zone at the next revolution. An average heat input over one revolution will be used to calculate the temperature rise of the body at the steady state.

The heat input is due to the heat generated at the instantaneous contact ellipse, and the amount depends on the load and the shear force of the lubricant. The heat flux flowing out of the body is due to the heat convection to surrounding air and lubricant. The relative importance of the heat-transfer coefficient at different surface areas was discussed by Patir and Cheng and Townsend and Akin (refs. 10 and 11) in spur gear systems. They also revealed the significant effect of lubrication method on temperature distribution. In this study, the oil-jet impingement depth is assumed to cover the whole area of contact side, which can be obtained by using a properly placed pressurized oil jet. The heat-transfer coefficients at other various areas are estimated to calculate the bulk temperature.

A three-dimensional, finite-element program is used to calculate the temperature coefficient. The mesh of the system includes gear shaft, gear body, and contact tooth with one adjacent tooth in both sides. The eight node element, which is used for the elastic deflection, is also used here for the bulk temperature. However, the boundary conditions are different. In the temperature analysis all surfaces are subject to heat convection with different heat-transfer coefficients.

The heat-transfer coefficient h_j is assigned to the contacting tooth face which is oil-jet cooled. The top land, bottom land, and another side of the tooth surface, which are not cooled by the oil jet,

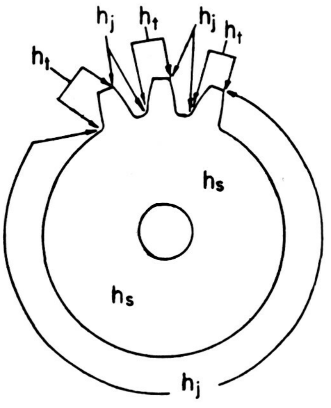

Figure 20. - Convective heat transfer coefficients for a three-tooth model for a spiral-bevel gear or pinion.

have a heat-transfer coefficient h_t for air or air/oil mist. Since only three teeth are made in the model, there is a surface region A (fig. 20) that covers the surfaces where the teeth are taken off and the bottom land which is in between these teeth. The heat-transfer coefficient at this region A is given a value h_j, which is the same as that of the coefficient for the surface cooled by the oil jet. The reason is that, because there is an oil-jet-cooled surface on each tooth, ~~and~~ most of the heat will flow out of the tooth from this surface ($h_j >> h_t$). All the other convective surfaces of the gear system are given a coefficient h_s (fig. 20). The theoretically estimated values of h_s and h_j can be found in references 12 and 13. However, the estimated values of h_s, h_j, and h_t, based on the experimental results (ref. 11), are used in this study.

There are 30 nodes created in the contacting surface. A unit heat flux is applied to the grid node i. The temperature distribution in this surface due to the heat flux is T_{ji}, which is the temperature at the grid node j due to the heat flux at node i. By the interpolation method, the temperature at the contact point m, due to the unit heat flux at the contact point n (T^c_{mn}) can be obtained in terms of T_{ji}. Once the contact path is located and the heat flux flowing into each body at each contact point is calculated, the bulk temperature at the contact point m can be found as

$$T_{m,B} = \sum T^c_{mn} Q_n \qquad n = 1, \ldots, k_{\max}$$

where $k_{\max}$ is the total number of contact points along the contact path.

The heat generation term Q_n is based on the recent traction models developed for EHL contacts by Johnson and Tevaarwerk (ref. 14), Bair and Winer (ref. 15), and Dyson (ref. 16). All three models are incorporated as subroutines in the bulk temperature calculation. Because there is a lack of the rheological constants for gear oils in the Johnson and Tevaarwerk's model and Bair and Winer's model, the limiting shear stress formula developed by Dyson for mineral oils in general is used first to obtain some preliminary results for the bulk temperature.

Flash Temperature

During meshing each tooth face experiences a sudden temperature increase (flash temperature) due to the frictional heat developed at the contact moving along the tooth face. This temperature rise is restricted in the instantaneous contact area and disappears very rapidly as soon as this instantaneous area of tooth face is out of contact. Usually, this temperature is very high and is a contributor to the gear scuffing failure.

The first successful prediction of flash temperature, introduced by Blok (ref. 17), is based on the heat-conduction analysis in a semi-infinite body with a uniformly distributed moving heat source. Jaeger (ref. 18) solved the problem of a moving source of heat with variable heat source and variable velocity. Archard introduced a simple harmonic mean to obtain the interface temperature. A refined solution including a local heat partition coefficient between a pair of disks was derived by Cameron, et al. (ref. 19). More recently, Francis (ref. 20) made a further refinement in Blok's calculation by considering a variable heat flux in the contact.

Archard showed that when the Peclet number, vR/a, is greater than 10, the heat flow in the direction perpendicular to sliding may be neglected. The temperature distribution within a heat source of finite area can be determined by dividing the whole contact area into differential strips parallel to the sliding direction. And the temperature profile along each strip is the same as that of an infinitely long band source (in the perpendicular direction to sliding) of width equal to the strip length and has the same heat flux profile along the strip.

For the division of heat between the two contacting surfaces, an average heat partition factor is used throughout the entire contact region. The average heat partition factor is determined by a method suggested by Francis (ref. 20) for a thin film with heat generated at the midfilm. Once the average partition factor is known, the flash temperature within each strip is calculated by the method suggested by Cameron, et al., (ref. 19) assuming a uniform heat source within the strip. Details of this procedure are documented (ref. 2).

Results of Lubrication Performance

The same set of gears used for the dynamic load calculation are used here to demonstrate calculation of lubrication performance. Results were obtained for a range of operating conditions to determine the effect of speed, load, lubricant viscosity, and ambient temperature on the film thickness, bulk temperature, and flash temperature. A sample of results is presented here. More complete results can be found in reference 2.

The sliding velocity decreases from the beginning of the contact path where the gear tip contacts the pinion root, until the contact point is near the pitch point where the sliding velocity becomes zero. Then the sliding velocity increases all the way to the end of the contact path where the pinion tip contacts the gear root. The current set of gears has the feature that the sliding velocity at the end of the contact path is larger than that at the beginning of the contact path; this fact creates a situation that more heat is generated at the end of the contact path.

A typical distribution of bulk temperature along the contact position is shown in figure 21. The bulk temperature of the pinion is always larger than that of the gear because the pinion speed is three times faster than the gear speed and receives more heat per unit time than the gear does. Although the temperature coefficients are higher near the gear tip, the maximum bulk temperature of both gears occurs at the end of the single-tooth contact point where the maximum heat is generated. A distribution of the total flash temperature for the same case is plotted in figure 22. The minimum flash temperature occurs at the pitch point where the sliding velocity is zero. For this high-speed case the variation of dynamic load is less pronounced along the contact path. The rise of flash temperature on both sides of the pitch corresponds directly to the variation of sliding speed at the contact. The slight decrease at the end of the contact path is attributable to the decrease in dynamic load in this region.

Figure 23 shows the distributions of film thickness for four different gear speeds. No excessive variations are seen along the contacting path. A moderate peak is evident at the pitch point for the high-speed cases, and this is associated with the slight drop of bulk temperature at the pitch point. The steady rise of film thickness along the contact path is due to the increase in the entrainment velocity. The final uptrend of film thickness near the end of contact is again due to the decrease in bulk temperature.

Finally, the effect of increase in ambient viscosity on the minimum film thickness, $h_{\min}$, maximum bulk temperature as well as total flash temperature is demonstrated in figure 24. As expected, an increase in viscosity would improve lubrication performance with a much thicker film thickness and a slight drop in both bulk and flash temperature.

Concluding Remarks

A computer solution to the dynamic load in a pair of spiral-bevel gearsets was developed by

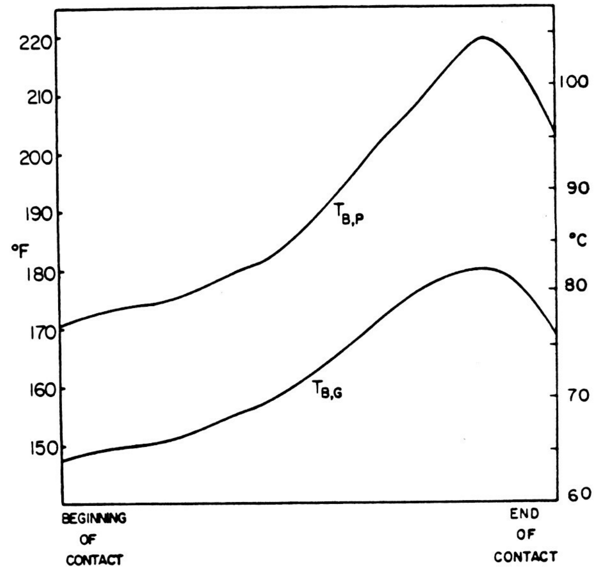

Figure 21. - Typical bulk temperature distribution for pinion and gear. Contact position, ω_g, 523 rad/sec.

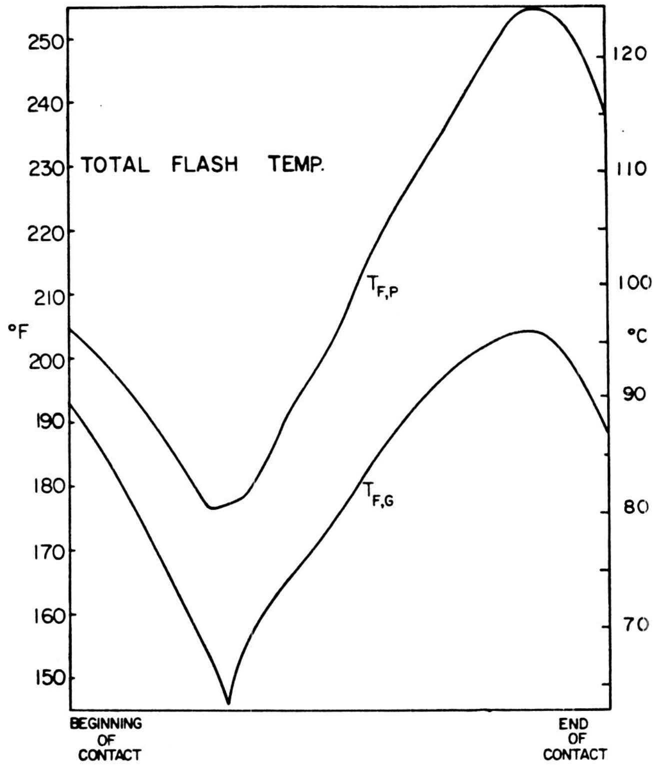

Figure 22. - Typical total flash temperature distribution for pinion and gear. Contact position, ω_g, 523 rad/sec.

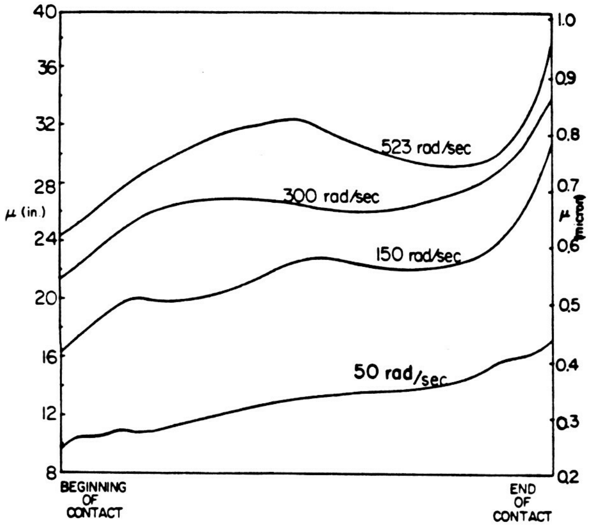

Figure 23. - Film thickness distributions.

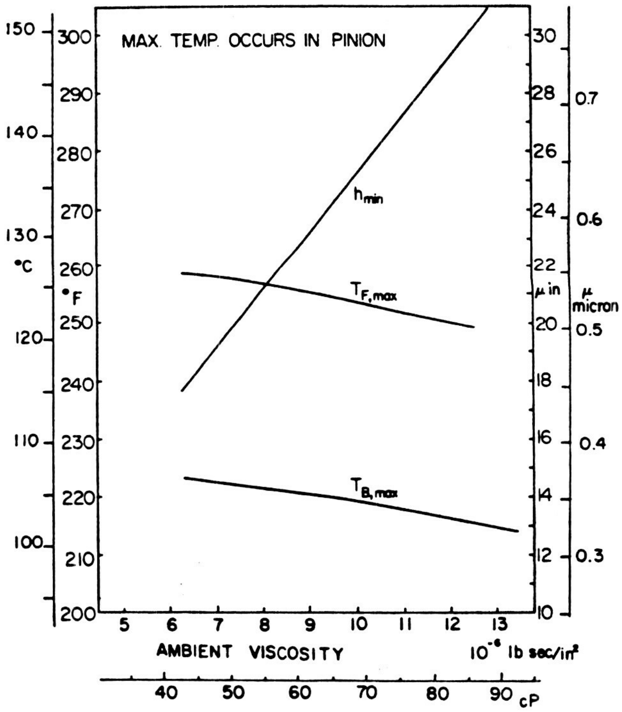

Figure 24. - Effect of lubricant viscosity on lubrication performance.

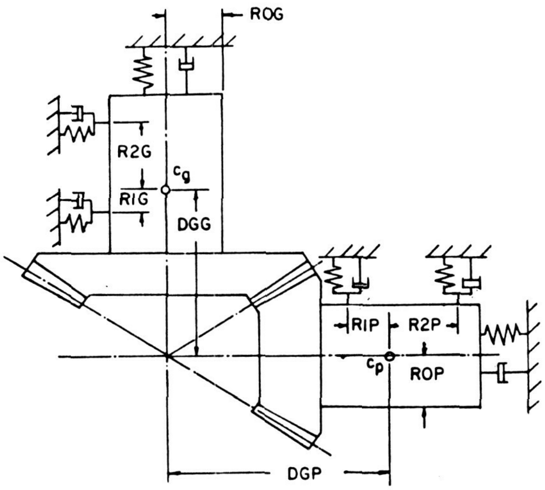

Figure 25. - Labels for distances between pinion and gear, mass centers to bearing supports.

solving the equations of motion for the pinion and gear shaft. An existing finite-element code was used to calculate the combined stiffness of the contacting pinion and gear teeth as a function of contacting position in the zone of action. In addition to the dynamic load analysis, a computer solution was also developed to predict the bulk surface temperature, the flash temperature, and the film thickness along the contact path. An existing finite-element heat code was also used to calculate the temperature influence coefficients from which the bulk surface temperature is calculated. Both the lubricant film thickness and the sliding traction are calculated from the recent findings in EHL theories.

Results were obtained for a set of experimental spiral-bevel gear currently being tested at the NASA Lewis Research Center. The results of dynamic load tests show that there exist numerous peaks in the variation of dynamic load against the gear shaft speed. These fluctuations correspond reasonably well with the critical frequencies of the system. The envelope of the peaks suggests that the highest dynamic load occurs somewhere near the critical frequency corresponding to the rotational mode oscillations of the two gears.

Results of the film thickness show that its variation along the contact path is not large and that it is caused mainly by the increase in the entrainment velocity and the change in bulk surface temperature. The total flash temperature variation is controlled by the sliding velocity and has its maximum near the end of the contact path where the transition from double to single mesh occurs. Effects of operating variables on the minimum film thickness and maximum surface temperatures along the contact path can also be obtained readily with this program. Results for the effect of ambient viscosity show trends consistent with those anticipated from existing EHL theories.

References

1. Goldstein, H.: Classical Mechanics. Addison-Wesley, 1960.
2. Chao, H. C.; and Cheng, H. S.: Dynamic Load, Lubricant Film Thickness, and Surface Temperatures in Spiral Bevel Gears. To appear as a NASA Contract Report.
3. Chao, H. C.: Tooth Profile and Contact Pattern of Spiral-Bevel Gears. M.S. Thesis, Northwestern University, Sept. 1979.
4. Wang, K. L.: Thermal Elastohydrodynamic Lubrication of Spur Gears. Ph.D. Dissertation, Northwestern University, Apr. 1976.
5. Wallace, D. W.; and Seireg, A.: Computer Solution of Dynamic Stress, Deformation and Fracture of Gear Teeth. J. Eng. Ind., Nov. 1973.
6. Wang, K. L.; and Cheng, H. S.: A Numerical Solution to the Dynamic Load, Film Thickness, and Surface Temperatures in Spur Gears. Part I—Analysis. J. Mech. Des., vol. 103, Jan. 1981, pp. 177-187.
7. Wang, K. L.; and Cheng, H. S.: A Numerical Solution to the Dynamic Load, Film Thickness, and Surface Temperatures in Spur Gears. Part II—Results. J. Mech. Des., vol. 103, Jan. 1981, pp. 188-194.

8. Hamrock, B. J.; and Dowson, D.: Isothermal Elastohydrodynamic Lubrication of Point Contact, Part II. J. Lubr. Technol., July, 1976.
9. Dowson, D.; and Higginson, G. R.: Elastohydrodynamic Lubrication. Pergamon Press, Ltd., 1966.
10. Patir, N.: Estimate of the Bulk Temperature in Spur Gears Based on Finite Element Temperature Analysis. M.S. Thesis, Northwestern University, Aug. 1976.
11. Townsend, D. P.; and Akin, L. S.: Analytical and Experimental Spur Gear Tooth Temperature as Affected by Operating Variables. J. Mech. Des., Jan. 1981, pp. 219–226.
12. DeWinter, A.; and Blok, H.: Fling-off Cooling of Gear Teeth, J Eng. Ind. vol. 96, no. 1, 1974.
13. Van Heijningen, G. J. J.; and Blok, H.: Continuous As Against Intermittent Fling-off Cooling of Gear Teeth. J. Lubr. Technol., vol. 96, no. 4, 1974.
14. Johnson, K. L.; and Tevaarwerk, J. L.: Shear Behavior of EHD Oil Film. Proc. Roy. Soc. (London), Ser. A, vol. 356, 1977.
15. Bair, S.; and Winer, W. O.: Shear Strength Measurements of Lubricant at High Pressure. J. Lubr. Technol., vol. 101, 1979.
16. Dyson, A.: Friction Traction and Lubrication Rheology in EHD Lubrication. Philos. Trans. Roy. Soc. (London), ser. A., vol. 266, 1970.
17. Blok, H.: Theoretical Study of Temperature Rise at Surfaces of Actual Contact Under Oiliness Lubricating Conditions. Proc. Inst. Mech. Engrs., Pt. 2, 1973.
18. Jaeger, J. C.: Moving Sources of Heat and Temperature at Sliding Contact. Proc. Roy. Soc. N.S.W. 76, 1942.
19. Cameron, A.; Gordon, A. N.; and Symm, G. T.: Contact Temperature in Rolling and Sliding Surfaces. Proc. Roy. Soc., A286, 1965.
20. Francis, H. A.: Interfacial Temperature Distribution Within a Sliding Hertzian Contact. Trans. ASLE, vol. 14, 1970.